

# Structure and Magnetism of the New Cage-structured Compound $\text{HfMn}_2\text{Zn}_{20}$

Nusrat Yasmin<sup>1</sup>, Md. Fahel Bin Noor<sup>1</sup>, and Tiglet Besara<sup>1,\*</sup>

<sup>1</sup> Department of Physics, Astronomy, and Materials Science, Missouri State University,  
Springfield, MO 65897, USA

## Abstract

A new cage-structured compound –  $\text{HfMn}_2\text{Zn}_{20}$  – belonging to the  $AB_2C_{20}$  ( $A, B$  = transition or rare earth metals, and  $C$  = Al, Zn, or Cd) family of structures has been synthesized via the self-flux method. The new compound crystallizes in the space group  $Fd\bar{3}m$  with lattice parameter  $a \approx 14.0543(2)$  Å ( $Z = 8$ ) and exhibits non-stoichiometry due to Mn/Zn mixing on the Mn-site and an underoccupied Hf-site. The structure refines to  $\text{Hf}_{0.93}\text{Mn}_{1.63}\text{Zn}_{20.37}$  and follows lattice size trends when compared to other  $\text{HfM}_2\text{Zn}_{20}$  ( $M$  = Fe, Co, and Ni) structures. The magnetic measurements show that this compound displays a modified Curie-Weiss behavior with a transition temperature around 22 K. The magnetization shows no saturation, a small magnetic moment, and near negligible hysteresis, all signs of the itinerant magnetism.

## Introduction

The large family of isostructural ternary intermetallic compounds with formula  $AB_2C_{20}$  ( $A, B$  = transition or rare earth metals, and  $C$  = Al, Zn, or Cd) crystallize in the  $\text{CeCr}_2\text{Al}_{20}$ -type structure [1] with space group  $Fd\bar{3}m$  and exhibit “cages” formed by the element  $C$  which contain the loosely-bound elements  $A$  and  $B$  [2-4]. There are over a hundred compounds in this 1-2-20 family and many of them have been explored for their magnetic behavior [5-24] and superconductivity [25-29], although most recently, the interest has been due to their enhanced low-temperature thermoelectricity [30-32]. With regards to their magnetic properties, the compounds which have Mn as the  $B$  element have been shown to exhibit itinerant magnetism [13,16,19,24,33]. Interestingly, the  $AMn_2Zn_{20}$  compounds have all been reported as non-stoichiometric: while Al or In was added to the  $AMn_2Zn_{20}$  ( $A$  = Y, Ce, Pr, Nd, Sm, Gd, Dy, Er, Yb) resulting in Al/Zn or In/Zn mixing [13,19,34], the  $\text{ZrMn}_2\text{Zn}_{20}$  exhibits a mixed Mn/Zn site [24], i.e., Zn residing in the Mn-site within a cage.

Here, we report on the discovery, single crystal growth, and magnetic properties of a new compound in this family,  $\text{HfMn}_2\text{Zn}_{20}$ , which, similar to its Zr analog, exhibits Mn/Zn mixing. We show that the structure of this new compound follows the expected lattice size trend when compared to the existing  $\text{HfM}_2\text{Zn}_{20}$  ( $M$  = Fe, Co, and Ni) [3] with deviations that can be explained by the Mn/Zn mixing. In addition, our magnetic study confirms the itinerant nature of this compound.

## Methods

*Synthesis.* Single crystals of  $\text{HfMn}_2\text{Zn}_{20}$  were grown via the self-flux method. Elements (>99.9%) were measured in atomic ratio of 1:2:60 Hf:Mn:Zn and loaded in a 2 ml alumina crucible, where the excess zinc acts as flux and provides enough reaction bath despite its boil-off at higher temperatures. A second alumina crucible was filled with quartz wool and put as a cap on the top of the reaction crucible. The two crucibles were then placed in a quartz ampoule. To ensure inert conditions of the reaction, the entire assembly was done inside an argon-filled glovebox. The quartz ampoule was subsequently sealed under vacuum using an oxygen-hydrogen torch and put inside a muffle furnace. The reaction was heated up at 800°C at a rate of 80°C/h, maintained at 800°C for 20 hours, and then slowly cooled to 550°C at a rate of 3°C/h. After completion of the temperature cycle, the quartz ampoule was rapidly taken out of the furnace, flipped upside down, and centrifuged to segregate the crystal from excess molten flux. After centrifuging and cooling, the quartz was broken to extract the crystals from inside the crucible. The extracted crystals had a layer of extra flux on their surface which was etched away with highly dilute HCl solution which attack elemental zinc at a higher rate than the crystals.

*Energy dispersion spectroscopy.* For energy dispersive spectroscopy (EDS)-based elemental analysis, a FEI QUANTA 200 FEG scanning electron microscope (SEM) equipped with an Oxford Instruments Ultim Max EDS detector was used. Several crystals of different sizes and shapes were picked to confirm the stoichiometry of the compound. All the crystals were fixed on copper tape so that a flat surface faced up.

*X-ray diffraction.* Single-crystal X-ray diffraction was performed with a Rigaku-Oxford Diffraction XtaLAB Synergy-S diffractometer equipped with a HyPix-6000HE Hybrid Photon Counting detector and dual PhotonJet-S Mo/Cu 50W Microfocus X-ray sources. Data were collected at room temperature with Mo  $K\alpha$  radiation ( $\lambda = 0.71073 \text{ \AA}$ ) using  $\omega$  scans with 0.5° frame widths to a resolution of 0.5 Å, equivalent to  $2\theta \approx 90^\circ$ . Reflections were recorded, indexed, and corrected for absorption using Rigaku Oxford Diffraction CrysAlisPro [35]. The structure refinement was done with CRYSTALS [36], employing the charge-flipping software SUPERFLIP [37] to solve the structure. The data quality permitted an unconstrained full matrix refinement against  $F^2$  with anisotropic displacement parameters for all atoms. A CIF has been deposited with the Cambridge Crystallographic Data Center (CSD #2212294) [38].

*Magnetization.* Magnetic measurements were done in a Quantum Design MPMS-3 system at the Cornell Center for Materials Research. Magnetization as a function of temperature was obtained at an applied field of 0.1 T and the temperature was swept at a rate of approximately 0.1 K/s. Magnetization as a function of field was obtained at temperatures

1.8 K and 300 K and the field was swept at a rate of approximately 50 Oe/s. All measurements were done with a zero field-cooled single crystal of approximately 14.6 mg.

## Result and discussion

### Structure

Several crystals of various sizes were grown out of the flux. The crystals exhibit, in general, an octahedral morphology (double pyramid shape), with the largest crystal approximately 1.5 mm long. Single crystal X-ray diffraction reveals that this compound crystallizes in the cubic space group  $Fd\bar{3}m$  ( $Z = 8$ ), isostructural with all other members of the  $AB_2C_{20}$  family [2,3]. The unit cell comprises large cages, or voids, of Zn with Hf in the center of a 16-atom coordinated Frank-Kasper polyhedron (twelve Zn1 and four Zn3) and Mn in the center of a 12-coordinated icosahedron (six Zn1 and six Zn2). All cages are corner-shared via the Zn1 atoms. The structure has been described in detail elsewhere [2,3,24,31]. Figure 1(a) shows the unit cell viewed along  $[110]$  with the Frank-Kasper polyhedra in blue and the icosahedra in purple. Figure 1(b) shows an image of the crystal, obtained with a scanning electron microscope.

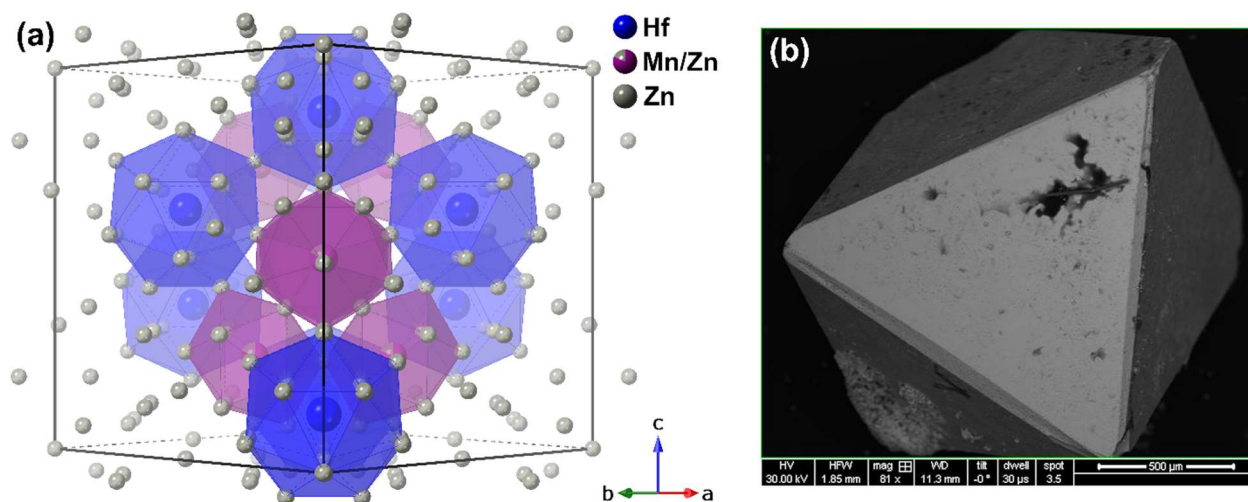


Figure 1. (a) Unit cell of  $HfMn_2Zn_{20}$  viewed along  $[110]$ . The structure image was generated with CrystalMaker [39]. (b) SEM image of a crystal of  $HfMn_2Zn_{20}$ .

The initial structural refinement based on the stoichiometric ratios resulted in good residuals ( $R_1 = 0.0273$  and  $wR_2 = 0.0723$ ), however, the elemental composition as obtained via EDS deviated enough from the stoichiometric 1:2:20 of  $HfMn_2Zn_{20}$  to raise concerns, despite the fairly large error margin of EDS. Furthermore, Svanidze *et al.* [24] reported off-stoichiometry in the Zr-analog,  $ZrMn_{1.78}Zn_{20.22}$ , which exhibited Mn/Zn site mixing on the 16d site (the Mn site). We performed EDS measurements on several spots and areas

on multiple crystals, and the average results are summarized in Table 1 together with calculated standard error of the mean. As can be seen, the Hf average value is within the ideal value. Mn, on the other hand, is lacking, and Zn is in excess. The EDS thus indicates a composition of  $\text{Hf}_{1.03 \pm 0.05} \text{Mn}_{1.75 \pm 0.03} \text{Zn}_{20.21 \pm 0.04}$ .

Table 1: Averages of the EDS results obtained on multiple crystals together with ratios based on the ideal 1:2:20 composition.

Elements	Atomic percentage	Ideal ratios
Hf	$4.5 \pm 0.2$	4.349
Mn	$7.6 \pm 0.1$	8.696
Zn	$87.9 \pm 0.2$	86.96
Composition	$\text{Hf}_{1.03 \pm 0.05} \text{Mn}_{1.75 \pm 0.03} \text{Zn}_{20.21 \pm 0.04}$	$\text{HfMn}_2\text{Zn}_{20}$

Further refinement on the X-ray diffraction data revealed indeed a Mn/Zn mixing on the 16d site. Unlike the Zr-analog, however, we also observe an underoccupied 8a site (the Hf site). It is not uncommon to observe Zr mixing in Hf sites since there is typically a nominal amount of Zr in Hf chemicals. EDS, however, revealed no Zr. It is not clear why the Hf site is underoccupied as there is no clear reason for Zn to site-mix with Hf. Nevertheless, the residuals improved remarkably and all the crystal data and crystallographic parameters resulting from the single-crystal X-ray diffraction are summarized in Table 2. The final composition refined to  $\text{Hf}_{0.93} \text{Mn}_{1.63} \text{Zn}_{20.37}$  ( $\text{Hf}_{1-\delta} \text{Mn}_{2-x} \text{Zn}_{20+x}$ ,  $\delta = 0.07$ ,  $x = 0.37$ ) which is fairly close to the composition found via EDS. For clarity, however, this compound will henceforth be referred to as  $\text{HfMn}_2\text{Zn}_{20}$ . Table 3 lists the atomic coordinates.

Table 2: Single crystal X-ray diffraction data and parameters for  $\text{HfMn}_2\text{Zn}_{20}$ , collected at room temperature.

Parameters	$\text{HfMn}_2\text{Zn}_{20}$
Actual stoichiometry	$\text{Hf}_{0.93} \text{Mn}_{1.63} \text{Zn}_{20.37}$ ( $\text{Hf}_{1-\delta} \text{Mn}_{2-x} \text{Zn}_{20+x}$ , $\delta = 0.07$ , $x = 0.37$ )
Molecular weight (g/mol)	1587.61
Space group	$Fd\bar{3}m$ (#227)
$a$ (Å)	14.0543(2)
$V$ (Å <sup>3</sup> )	2776.03(9)
$Z$	8
$\rho_{\text{calc}}$ (g/cm <sup>3</sup> )	7.597
Absorption coefficient $\mu$ (mm <sup>-1</sup> )	42.744
Absorption corrections $T_{\text{min}}$ , $T_{\text{max}}$	0.22, 0.30
Crystal size (mm <sup>3</sup> )	0.028 x 0.041 x 0.050

Data collection range (°)	$2.510 < \theta < 44.778$
$h$ range	$-19 \leq h \leq 27$
$k$ range	$-27 \leq k \leq 16$
$l$ range	$-27 \leq l \leq 19$
Reflections collected	5375
Independent reflections	587
Parameters refined	18
Restraints	6
$\Delta\rho_{\min}, \Delta\rho_{\max}$ (e/Å <sup>-3</sup> )	-6.36, 3.01
$R_{\text{int}}$	0.023
$R_1(F)$ for all data <sup>a</sup>	0.0176
$wR_2(F_o^2)^b$	0.0305
Goodness-of-fit on $F^2$	1.0000
CSD #	2212294

<sup>a</sup>  $R_1 = \Sigma \|F_o\| - \|F_c\| / \Sigma \|F_o\|$ .

<sup>b</sup>  $wR_2 = [\Sigma w(F_o^2 - F_c^2)^2 / \Sigma w(F_o^2)^2]^{1/2}$ ,  $w = 1/[\sigma^2(F_o^2) + (A \cdot P)^2 + B \cdot P]$ ,  $P = [2F_c^2 + \text{Max}(F_o^2, 0)]/3$  where  $A = 0.01$  and  $B = 22.81$ .

Table 3. Atomic coordinates, and equivalent displacement parameters of HfMn<sub>2</sub>Zn<sub>20</sub>.

Atom	Site	SOF	x	y	z	$U_{\text{eq}}$ (Å <sup>2</sup> )
Hf	8a	0.932(2)	1/8	1/8	1/8	0.0063(5)
Mn11	16d	0.816(9)	1/2	1/2	1/2	0.0056(4)
Zn12	16d	0.184(9)	1/2	1/2	1/2	0.0056(4)
Zn1	96g	1	0.06010(2)	0.06010(2)	0.32312(2)	0.0132(9)
Zn2	48f	1	0.48833(2)	1/8	1/8	0.0090(1)
Zn3	16c	1	0	0	0	0.0148(1)

Gross *et al.* [3] compared the structural parameters of several HfM<sub>2</sub>Zn<sub>20</sub> compounds including  $M = \text{Fe, Co, and Ni}$  where they showed a lattice constant and unit cell volume reduction consistent with the metallic radius trend of the transition metals [40]. We extend the trend with the addition of HfMn<sub>2</sub>Zn<sub>20</sub>. Figure 2 displays the trend in lattice parameter and unit cell volume of HfM<sub>2</sub>Zn<sub>20</sub> for  $M = \text{Mn, Fe, Co, and Ni}$ . While the metallic radius increases linearly from 1.24 Å for Ni to 1.27 Å for Mn [40], the lattice parameter and the unit cell volume are larger for our HfMn<sub>2</sub>Zn<sub>20</sub> compound than expected from the linear trend. The reason for this deviation could be due to the Mn/Zn site mixing: the metallic radius of Zn is 1.34 Å, approximately 8.1% larger than the metallic radius of Mn, so that the inclusion of Zn on the Mn-site enlarges the overall unit cell of HfMn<sub>2</sub>Zn<sub>20</sub> more than expected.

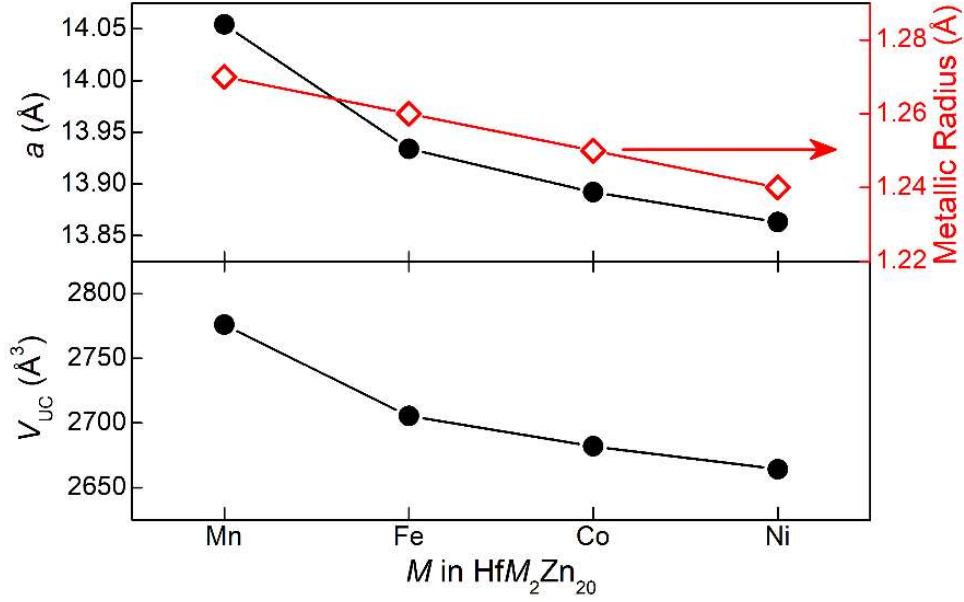


Figure 2: Lattice constant (upper panel) and unit cell volume (lower panel) comparison for  $\text{HfM}_2\text{Zn}_{20}$  (red circles) across  $M = \text{Mn}, \text{Fe}, \text{Co},$  and  $\text{Ni}$ . The metallic radii are shown on the right axis of the upper panel (open, red diamonds) [40]. Data for the  $M = \text{Fe}, \text{Co},$  and  $\text{Ni}$  compounds are taken from Ref. [3]. All error bars are within symbols.

In fact, looking at the volumes of the two polyhedra, we can observe the deviation of the Mn/Zn-containing icosahedron from the linear trend (upper panel in Figure 3). The Frank-Kasper polyhedron containing Hf, on the other hand, shrinks when  $M$  goes from Fe to Mn (lower panel in Figure 3). One reason could be the underoccupied Hf-site, although it is more likely that the overall structure is the real reason: a Frank-Kasper polyhedron is corner-shared with 12  $M$ -containing icosahedra and only four other Frank-Kasper polyhedra. The Frank-Kasper polyhedron is therefore affected strongly by the relatively larger expansion of the surrounding icosahedra; hence, it is compressed.

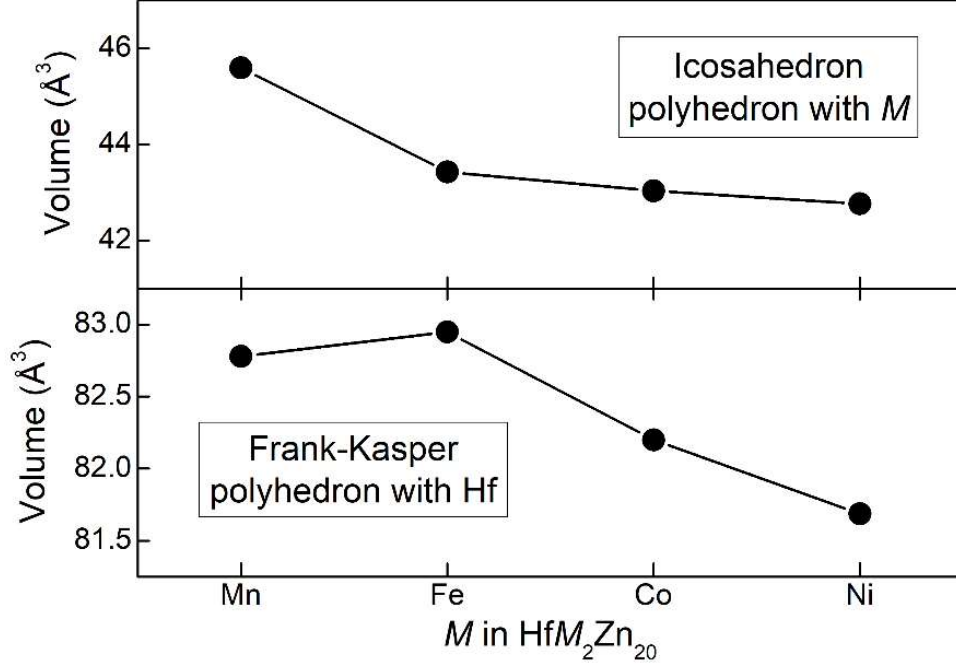


Figure 3: Volume of the icosahedron that contains the  $M$  atom (upper panel) and volume of the Frank-Kasper polyhedron that contains Hf (lower panel) across  $\text{HfM}_2\text{Zn}_{20}$  with  $M = \text{Mn}, \text{Fe}, \text{Co},$  and  $\text{Ni}$ . Data for the  $M = \text{Fe}, \text{Co},$  and  $\text{Ni}$  compounds are taken from Ref. [GROSS]. All error bars are within symbols.

#### Magnetic properties

Figure 4 displays the zero field-cooled magnetic susceptibility as a function of temperature at an applied field of 0.1 T. The derivative (solid line) indicates two transitions: one at approximately 22.3 K and one at approximately 8.7 K with the lower transition temperature possibly due to ferromagnetic impurities. The susceptibility clearly shows a non-Curie-Weiss behavior. The lack of Curie-Weiss behavior together with two transitions were also observed in the  $\text{ZrMn}_2\text{Zn}_{20}$  analog [24] where it was also noted that these behaviors were reminiscent of other compounds containing Mn [41]. The susceptibility, in fact, seems to follow the modified Curie-Weiss behavior [42]

$$\chi = \frac{C}{T - \theta} + \chi_0 \quad (1)$$

in the region above the transition temperature (inset to Figure 4). Here,  $\theta$  is a Curie-Weiss temperature,  $\chi_0$  is a temperature-independent term, and  $C$  is the Curie constant and is related to the effective moment  $\mu_{\text{eff}}$  via

$$C = \frac{N_A \mu_B^2 \mu_{\text{eff}}^2}{3k_B}. \quad (2)$$

The susceptibility data above the transition temperature fits Eqs. (1) and (2) moderately well with the fit displayed in the inset to Figure 4 as a green, solid line. The fit yields the effective moment  $\mu_{\text{eff}} \approx 0.223(2) \mu_B/\text{f.u.}$ , the Curie-Weiss temperature  $\theta \approx 21.8(2) \text{ K}$ , and  $\chi_0 \approx 6.68(8) \cdot 10^{-4} \text{ emu/mol f.u.}$ , although the error margins are likely larger due to uncertainty in the mass of the sample. Nevertheless, the positive Curie-Weiss temperature indicates that the transition is of a ferromagnetic nature.

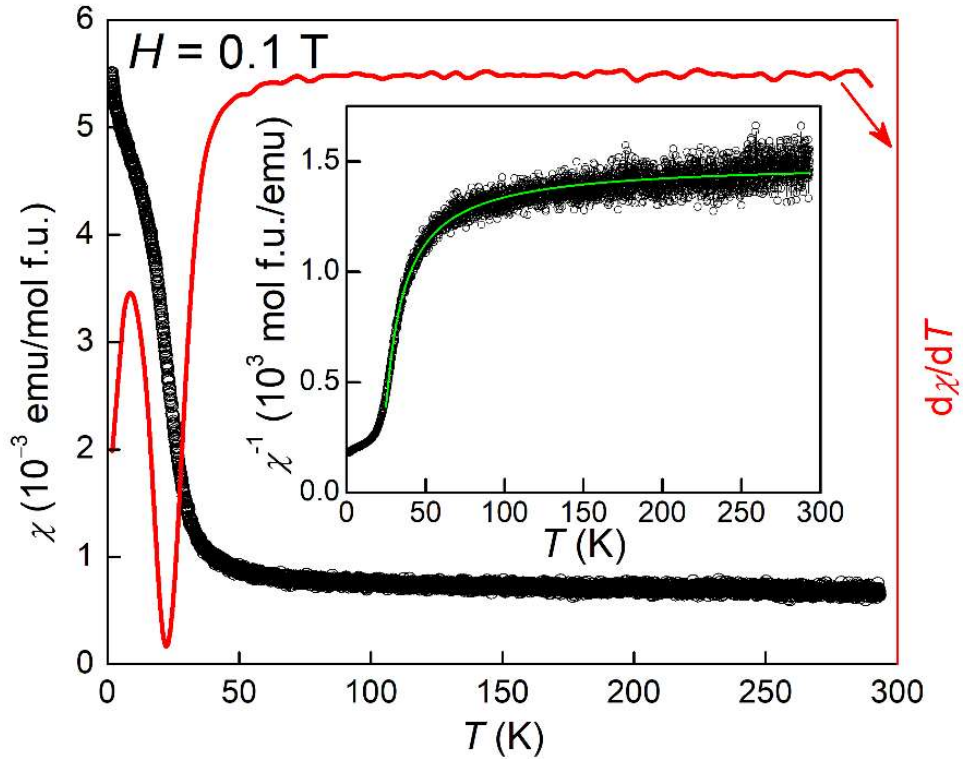


Figure 4: Zero field-cooled magnetic susceptibility as a function of temperature, obtained at an applied field of 0.1 T. The red solid line (right axis) is the derivative of the susceptibility, showing two transitions. Inset: inverse susceptibility as a function of temperature. The green solid line is a fit to the modified Curie-Weiss law.

Figure 5 displays the magnetization as a function of applied field at 1.8 K and at 300 K. No saturation is observed even at the lowest temperature (1.8 K) and highest applied field (6 T) and the moment at 1.8 K and 6 T is quite small: approximately  $0.01 \mu_B/\text{mol f.u.}$  In addition, hysteresis in the 1.8 K isotherm is very small, essentially negligible (upper inset to Figure 5). All of these – no saturation, small magnetic moment, and lack of hysteresis – have been taken as evidence for itinerant magnetism in the analogous  $\text{ZrMn}_2\text{Zn}_{20}$



compound [24,33].  $\text{HfMn}_2\text{Zn}_{20}$  is, therefore, a likely candidate for itinerant ferromagnetism.

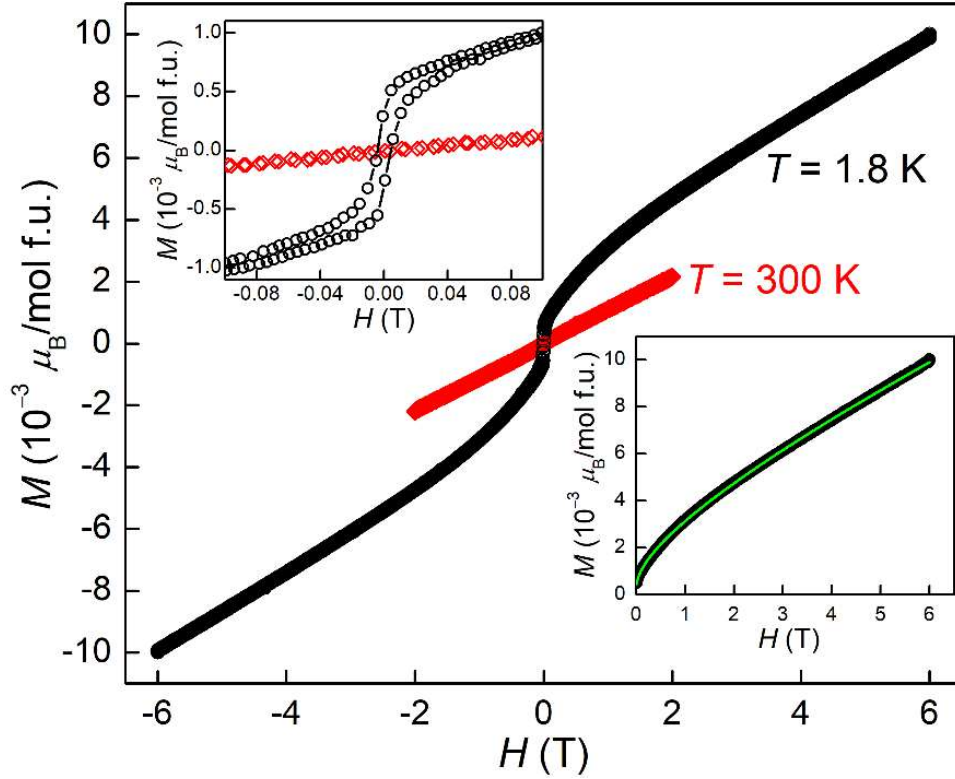


Figure 5: Magnetization as a function of applied field, obtained at 1.8 K (black circles) and 300 K (red diamonds). Upper inset: Close-up around zero showing the low-field saturation and the near-negligible hysteresis at 1.8 K. Lower inset: Magnetization curve above zero applied field. The solid green line is a fit to Eq. 3 (see main text).

The isotherm at 1.8 K experiences a small but steep rise (upper inset to Figure 5) before the so-called low-field saturation (the bend in the isotherm) sets in at approximately 0.015 T. The spontaneous magnetization at 1.8 K, i.e.,  $M_{\text{SP}} = M(H = 0)$  can be obtained by fitting  $M(H)$  above the low-field saturation to the expression [43,44]

$$M(H) = M_{\text{SP}} + a\sqrt{H} + \chi_{\text{hf}}H, \quad (3)$$

where the middle term is related to the field-suppression of spin waves and  $\chi_{\text{hf}}$  is the high-field susceptibility. The fit is displayed in the lower inset to Figure 5 as a green, solid line and the parameters are  $M_{\text{SP}} \approx 2.87(5) \cdot 10^{-4} \mu_{\text{B}}/\text{mol f.u.}$ ,  $a \approx 2.09(1) \cdot 10^{-3} \mu_{\text{B}}/\text{mol f.u.} \cdot \text{T}^{1/2}$ , and  $\chi_{\text{hf}} \approx 7.50(3) \cdot 10^{-4} \mu_{\text{B}}/\text{mol f.u.} \cdot \text{T}$ .

The itinerant magnetism of this sample can be analyzed with spin fluctuation theories [33,45-50] which built on the earlier Stoner criterion [51]. We will not venture too

deeply into the theory due to the limited magnetic measurements obtained; for a more complete analysis, Arrott plots ( $H/M$  vs.  $M^2$  plots) should be obtained at several temperatures to properly determine the critical temperature  $T_C$  and the slope of the Arrott curve at  $T_C$ . Instead, we note that out of these theories, the relation

$$\frac{\mu_{\text{eff}}}{\mu_S} \approx 1.4 \left( \frac{T_0}{T_C} \right)^{2/3} \quad (4)$$

is obtained which relates the effective moment  $\mu_{\text{eff}}$ , the spontaneous magnetic moment  $\mu_S$ , the critical temperature  $T_C$ , and the spin fluctuation parameter in energy space  $T_0$  [50,52,53]. The ratio  $\mu_{\text{eff}}/\mu_S$  can be rewritten as  $\mu_C/\mu_S$  where  $\mu_C$  is the paramagnetic moment and is related to the effective moment via  $\mu_{\text{eff}}^2 = \mu_C(\mu_C + 2)$ . The ratio  $\mu_C/\mu_S$  is the so-called Rhodes-Wohlfarth ratio [54] and for itinerant magnetic systems  $\mu_C/\mu_S \gg 1$  [33]. Using the effective moment obtained via Eqs. (1) and (2) and the spontaneous magnetic moment obtained via Eq. (3), we obtain a Rhodes-Wohlfarth ratio of approximately 85, hence indicating that  $\text{HfMn}_2\text{Zn}_{20}$  is indeed an itinerant magnetic system. Furthermore, the ratio  $T_C/T_0$  can predict the degree of localization [44,50]. If the ratio is equal to 1 the magnetism is governed by local moments, while if it is  $\ll 1$  the magnetic nature is strongly itinerant. Using the evaluated Rhodes-Wohlfarth ratio, Eq. (4) yields  $T_0 \approx 2.87 \cdot 10^5$  K. Using  $T_C \approx 22$  K (from Figure 4), it is clear that  $T_C/T_0 \ll 1$ , and, hence, the strongly itinerant nature of  $\text{HfMn}_2\text{Zn}_{20}$  is confirmed.

## Conclusion

In conclusion, we have discovered a new member of the  $AB_2C_{20}$  family:  $\text{HfMn}_2\text{Zn}_{20}$ . Due to Mn/Zn mixing on the Mn-site and an underoccupied Hf-site, the final stoichiometry is  $\text{Hf}_{0.93}\text{Mn}_{1.63}\text{Zn}_{20.37}$  ( $\text{Hf}_{1-\delta}\text{Mn}_{2-x}\text{Zn}_{20+x}$ ,  $\delta = 0.07$ ,  $x = 0.37$ ). This Mn-site mixing was also observed in the Zr-analog. The structure of the new compound follows expected lattice size trends when compared to existing isostructures with Hf and first-row transition metals. The magnetic susceptibility follows the modified Curie-Weiss law with a transition temperature around 22 K. The magnetization as a function of applied field shows no saturation, a small magnetic moment, and near negligible hysteresis, all signs of the itinerant nature of the magnetism in this compound.

## Acknowledgement

The authors acknowledge the NSF MRI program that funded the purchase of the Synergy-S X-ray diffractometer via award CHE-2117129. This work made use of a Quantum Design MPMS-3 supported by NSF (DMR-1920086) and the Cornell Center for Materials Research Shared Facilities which are supported through the NSF MRSEC

program (DMR-1719875). T.B. also acknowledges financial support provided by Missouri State University's new faculty startup fund.

## References

- [1] P. I. Kripyakevich and O. S. Zarechnyuk,  $\text{RCr}_2\text{Al}_{20}$  Compounds in Systems of Rare Earth Metals and Calcium, and their Crystal Structures, *Dopov. Akad. Nauk Ukr. RSR, Ser. A* 30, 364-367 (1968).
- [2] T. Nasch, W. Jeitschko, and U. C. Rodewald, Ternary Rare Earth Transition Metal Zinc Compounds  $\text{RT}_2\text{Zn}_{20}$  with  $T = \text{Fe, Ru, Co, Rh, and Ni}$ , *Z. Naturforsch. B* 52, 1023-1030 (1997).
- [3] N. Gross, T. Nasch, and W. Jeitschko, Ternary Intermetallics with High Zinc Content:  $\text{TT}'_2\text{Zn}_{20}$  ( $T = \text{Zr, Hf, Nb}$ ;  $T' = \text{Mn, Fe, Ru, Co, Rh, Ni}$ ) with  $\text{CeCr}_2\text{Al}_{20}$ -type Structure, *J. Solid State Chem.* 161, 288-293 (2001), 10.1006/jssc.2001.9311.
- [4] S. Niemann and W. Jeitschko, Ternary Aluminides  $\text{AT}_2\text{Al}_{20}$  ( $A = \text{Rare Earth Elements and Uranium}$ ;  $T = \text{Ti, Nb, Ta, Mo, and W}$ ) with  $\text{CeCr}_2\text{Al}_{20}$ -type Structure, *J. Solid State Chem.* 114, 337-341 (1995).
- [5] E. D. Bauer, A. D. Christianson, J. S. Gardner, V. A. Sidorov, J. D. Thompson, J. L. Sarrao, and M. F. Hundley, Physical Properties of the Ferromagnetic Heavy-fermion Compound  $\text{UIr}_2\text{Zn}_{20}$ , *Phys. Rev. B* 74, 155118 (2006), 10.1103/PhysRevB.74.155118.
- [6] S. Jia, S. L. Bud'ko, G. D. Samolyuk, and P. C. Canfield, Nearly Ferromagnetic Fermi-liquid Behaviour in  $\text{YFe}_2\text{Zn}_{20}$  and High-temperature Ferromagnetism of  $\text{GdFe}_2\text{Zn}_{20}$ , *Nature Phys.* 3, 334-338 (2007), 10.1038/nphys568.
- [7] S. Jia, N. Ni, S. L. Bud'ko, and P. C. Canfield, Magnetic Properties of  $\text{Gd}_x\text{Y}_{1-x}\text{Fe}_2\text{Zn}_{20}$ : Dilute, Large-S Moments in a Nearly Ferromagnetic Fermi Liquid, *Phys. Rev. B* 76, 184410 (2007), 10.1103/PhysRevB.76.184410.
- [8] Y. Verbovytsky, K. Łatka, and K. Tomala, The Crystal Structure and Magnetic Properties of the  $\text{GdV}_2\text{Al}_{20}$  and  $\text{GdCr}_2\text{Al}_{20}$  Ternary Compounds, *J. Alloy. Comp.* 442, 334-336 (2007), 10.1016/j.jallcom.2006.07.148.
- [9] S. Jia, N. Ni, G. D. Samolyuk, A. Safa-Sefat, K. Dennis, H. Ko, G. J. Miller, S. L. Bud'ko, and P. C. Canfield, Variation of the Magnetic Ordering in  $\text{GdT}_2\text{Zn}_{20}$  ( $T = \text{Fe, Ru, Os, Co, Rh and Ir}$ ) and Its Correlation with the Electronic Structure of Isostructural  $\text{YT}_2\text{Zn}_{20}$ , *Phys. Rev. B* 77, 104408 (2008), 10.1103/PhysRevB.77.104408.
- [10] P. C. Canfield, S. Jia, E. D. Mun, S. L. Bud'ko, G. D. Samolyuk, and M. S. Torikachvili, Myriad of Correlated Electron Effects Found in the  $\text{RT}_2\text{Zn}_{20}$  Family, *Phys. B: Condens. Matter* 403, 844-846 (2008), 10.1016/j.physb.2007.10.234.
- [11] S. Jia, N. Ni, S. L. Bud'ko, and P. C. Canfield, Magnetic Properties of  $\text{RFe}_2\text{Zn}_{20}$  and  $\text{RCo}_2\text{Zn}_{20}$  ( $R = \text{Y, Nd, Sm, Gd-Lu}$ ), *Phys. Rev. B* 80, 104403 (2009), 10.1103/PhysRevB.80.104403.
- [12] S. Yoshiuchi, M. Toda, M. Matsushita, S. Yasui, Y. Hirose, M. Ohya, K. Katayama, F. Honda, K. Sugiyama, M. Hagiwara, K. Kindo, T. Takeuchi, E. Yamamoto, Y. Haga, R.

- Settai, T. Tanaka, Y. Kubo, and Y. Ōnuki, Heavy Fermion State in  $\text{YbIr}_2\text{Zn}_{20}$ , *J. Phys. Soc. Jpn.* 78, 123711 (2009), 10.1143/jpsj.78.123711.
- [13] Y. Okamoto, T. Shimizu, J.-i. Yamaura, Y. Kiuchi, and Z. Hiroi, Itinerant-electron Magnet of the Pyrochlore Lattice: Indium-doped  $\text{YMn}_2\text{Zn}_{20}$ , *J. Phys. Soc. Jpn.* 79, 093712 (2010), 10.1143/JPSJ.79.093712.
- [14] W. Tian, A. D. Christianson, J. L. Zarestky, S. Jia, S. L. Bud'ko, P. C. Canfield, P. M. B. Piccoli, and A. J. Schultz, Magnetic Order in  $\text{TbCo}_2\text{Zn}_{20}$  and  $\text{TbFe}_2\text{Zn}_{20}$ , *Phys. Rev. B* 81, 144409 (2010), 10.1103/PhysRevB.81.144409.
- [15] C. H. Wang, A. D. Christianson, J. M. Lawrence, E. D. Bauer, E. A. Goremychkin, A. I. Kolesnikov, F. Trouw, F. Ronning, J. D. Thompson, M. D. Lumsden, N. Ni, E. D. Mun, S. Jia, P. C. Canfield, Y. Qiu, and J. R. D. Copley, Neutron Scattering and Scaling Behavior in  $\text{URu}_2\text{Zn}_{20}$  and  $\text{YbFe}_2\text{Zn}_{20}$ , *Phys. Rev. B* 82, 184407 (2010), 10.1103/PhysRevB.82.184407.
- [16] C. H. Wang, J. M. Lawrence, E. D. Bauer, K. Kothapalli, J. S. Gardner, F. Ronning, K. Gofryk, J. D. Thompson, H. Nakotte, and F. Trouw, Unusual Signatures of the Ferromagnetic Transition in the Heavy Fermion Compound  $\text{UMn}_2\text{Al}_{20}$ , *Phys. Rev. B* 82, 094406 (2010), 10.1103/PhysRevB.82.094406.
- [17] Y. Hirose, M. Toda, S. Yoshiuchi, S. Yasui, K. Sugiyama, F. Honda, M. Hagiwara, K. Kindo, R. Settai, and Y. Ōnuki, Metamagnetic Transition in Heavy Fermion Compounds  $\text{YbT}_2\text{Zn}_{20}$  ( $T: \text{Co, Rh, Ir}$ ), *J. Phys.: Conf. Ser.* 273, 012003 (2011), 10.1088/1742-6596/273/1/012003.
- [18] M. J. Kangas, D. C. Schmitt, A. Sakai, S. Nakatsuji, and J. Y. Chan, Structure and Physical Properties of Single Crystal  $\text{PrCr}_2\text{Al}_{20}$  and  $\text{CeM}_2\text{Al}_{20}$  ( $M=\text{V, Cr}$ ): A Comparison of Compounds Sadopting the  $\text{CeCr}_2\text{Al}_{20}$  Structure Type, *J. Solid State Chem.* 196, 274-281 (2012), 10.1016/j.jssc.2012.06.035.
- [19] Y. Okamoto, T. Shimizu, J. Yamaura, and Z. Hiroi, Crystal Chemistry and Magnetic Properties of Manganese Zinc Alloy “ $\text{YMn}_2\text{Zn}_{20}$ ” Comprising a Mn Pyrochlore Lattice, *J. Solid State Chem.* 191, 246-256 (2012), 10.1016/j.jssc.2012.03.038.
- [20] P. Swatek and D. Kaczorowski, Magnetic and Electrical Properties of  $\text{UCr}_2\text{Al}_{20}$  Single Crystals, *J. Solid State Chem.* 191, 191-194 (2012), 10.1016/j.jssc.2012.03.018.
- [21] N. Kase, Y. Shimura, S. Kittaka, T. Sakakibara, S. Nakatsuji, T. Nakano, N. Takeda, and J. Akimitsu, Antiferromagnetic Transition of the Caged Compound  $\text{TmTi}_2\text{Al}_{20}$ , *J. Phys.: Conf. Ser.* 592, 012052 (2015), 10.1088/1742-6596/592/1/012052.
- [22] K. Wakiya, K. T. Matsumoto, T. Onimaru, K. Umeo, and T. Takabatake, Ferromagnetic Transition in a Caged Compound  $\text{NdOs}_2\text{Zn}_{20}$ , *Phys. Procedia* 75, 511-515 (2015), 10.1016/j.phpro.2015.12.064.
- [23] Y. Hirose, H. Doto, F. Honda, D. Li, D. Aoki, Y. Haga, and R. Settai, New Heavy-fermion Antiferromagnet  $\text{UPd}_2\text{Cd}_{20}$ , *J. Phys.: Condens. Matter* 28, 425601 (2016), 10.1088/0953-8984/28/42/425601.

- [24] E. Svanidze, M. Kindy II, C. Georgen, B. W. Fulfer, S. H. Lapidus, J. Y. Chan, and E. Morosan, Magnetic and Crystallographic Properties of  $ZrM_{2-d}Zn_{20+d}$  ( $M = Cr-Cu$ ), *J. Magn. Magn. Mater.* 416, 401-407 (2016), 10.1016/j.jmmm.2016.04.082.
- [25] T. Onimaru, K. T. Matsumoto, Y. F. Inoue, K. Umeo, Y. Saiga, Y. Matsushita, R. Tamura, K. Nishimoto, I. Ishii, T. Suzuki, and T. Takabatake, Superconductivity and Structural Phase Transitions in Caged Compounds  $RT_2Zn_{20}$  ( $R = La, Pr, T = Ru, Ir$ ), *J. Phys. Soc. Jpn.* 79, 033704 (2010), 10.1143/jpsj.79.033704.
- [26] Z. Hiroi, A. Onosaka, Y. Okamoto, J. Yamaura, and H. Harima, Rattling and Superconducting Properties of the Cage Compound  $Ga_xV_2Al_{20}$ , *J. Phys. Soc. Jpn.* 81, 124707 (2012), 10.1143/jpsj.81.124707.
- [27] A. Onosaka, Y. Okamoto, J.-i. Yamaura, and Z. Hiroi, Superconductivity in the Einstein Solid  $A_xV_2Al_{20}$  ( $A = Al$  and  $Ga$ ), *J. Phys. Soc. Jpn.* 81, 023703 (2012), 10.1143/JPSJ.81.023703.
- [28] M. J. Winarski, B. Wiendlocha, M. Sternik, P. Wiśniewski, J. R. O'Brien, D. Kaczorowski, and T. Klimczuk, Rattling-enhanced Superconductivity in  $MV_2Al_{20}$  ( $M = Sc, Lu, Y$ ) Intermetallic Cage Compounds, *Phys. Rev. B* 93, 134507 (2016), 10.1103/PhysRevB.93.134507.
- [29] N. Nakamura, R. Higashinaka, Y. Aoki, H. Sato, and T. D. Matsuda, Superconducting Properties of Cage Compounds  $YbTr_2Al_{20}$  with  $Tr = Mo$  and  $Ta$ , *Solid State Commun.* 363, 115098 (2023), 10.1016/j.ssc.2023.115098.
- [30] E. D. Mun, S. Jia, S. L. Bud'ko, and P. C. Canfield, Thermoelectric Power of the  $YbT_2Zn_{20}$  ( $T = Fe, Ru, Os, Ir, Rh$ , and  $Co$ ) Heavy Fermions, *Phys. Rev. B* 86, 115110 (2012), 10.1103/PhysRevB.86.115110.
- [31] K. Wei, J. N. Neu, Y. Lai, K.-W. Chen, D. Hobbis, G. S. Nolas, D. E. Graf, T. Siegrist, and R. E. Baumbach, Enhanced Thermoelectric Performance of Heavy-fermion Compounds  $YbTM_2Zn_{20}$  ( $TM = Co, Rh, Ir$ ) at Low Temperatures, *Sci. Adv.* 5, eaaw6183 (2019), 10.1126/sciadv.aaw6183.
- [32] J. R. Galeano-Cabral, E. Karr, B. Schundelmier, O. Oladehin, E. S. Choi, T. Siegrist, J. Ordonez, S. Shastri, V. Petkov, R. E. Baumbach, and K. Wei, Enhanced Thermoelectric Properties of Heavy-fermion Compounds  $Yb_xCe_ySm_zIr_2Zn_{20}$  ( $x + y + z = 1$ ), *Phys. Rev. Mater.* 7, 025406 (2023), 10.1103/PhysRevMaterials.7.025406.
- [33] J. M. Santiago, C. L. Huang, and E. Morosan, Itinerant Magnetic Metals, *J. Phys.: Condens. Matter* 29, 373002 (2017), 10.1088/1361-648X/aa7889.
- [34] E. M. Benbow and S. E. Lattner, Mixed-metal Flux Synthesis of Quaternary  $RMn_2Tr_xZn_{20-x}$  Compounds with  $Tr = Al, In$ , *J. Solid State Chem.* 179, 3989-3996 (2006), 10.1016/j.jssc.2006.09.001.
- [35] P. o. t. R. S. o. L. S. A. M. a. P. Sciences, Rigaku Oxford Diffraction CrysAlisPro, version 1.171.42.53a, Rigaku Corporation, Oxford, England, 2022.

- [36] P. W. Betteridge, J. R. Carruthers, R. I. Cooper, K. Prout, and D. J. Watkin, CRYSTALS version 12: Software for Guided Crystal Structure Analysis, *J. Appl. Crystallogr.* 36, 1487 (2003), 10.1107/S0021889803021800.
- [37] L. Palatinus and G. Chapuis, SUPERFLIP - a Computer Program for the Solution of Crystal Structures by Charge Flipping in Arbitrary Dimensions, *J. Appl. Crystallogr.* 40, 786-790 (2007), 10.1107/S0021889807029238.
- [38] C. R. Groom, I. J. Bruno, M. P. Lightfoot, and S. C. Ward, The Cambridge Structural Database, *Acta Crystallographica B* 72, 171-179 (2016), 10.1107/S2052520616003954.
- [39] CrystalMaker, version 10.8.1, CrystalMaker Software Ltd, Oxford, England, 2023.
- [40] J. C. Slater, Atomic Radii in Crystals, *J. Chem. Phys.* 41, 3199-3204 (1964), 10.1063/1.1725697.
- [41] M. Shiga, H. Wada, K. Yoshimura, and Y. Nakamura, Transition from Itinerant Electron to Local Moment System in  $\text{Y}(\text{Mn}_{1-x}\text{Al}_x)_2$ , *J. Magn. Magn. Mater.* 54-57, 1073-1074 (1986), 10.1016/0304-8853(86)90387-2.
- [42] S. Mugiraneza and A. M. Hallas, Tutorial: a Beginner's Guide to Interpreting Magnetic Susceptibility Data with the Curie-Weiss Law, *Commun. Phys.* 5, 95 (2022), 10.1038/s42005-022-00853-y.
- [43] A. Semwal and S. N. Kaul, Magnetic Properties of the Weak Itinerant-electron Ferromagnet  $\text{Ni}_{75}\text{Al}_{25}$ : I. The Effect of Site Disorder, *J. Phys.: Condens. Matter* 16, 8675 (2004), 10.1088/0953-8984/16/47/019.
- [44] D. Patra, S. Vishvakarma, P. D. Babu, and S. Veeturi, Weak Itinerant Magnetic Behaviour in Al Substituted  $\text{Ni}_{92}\text{Cr}_8$  Alloys, *AIP Adv.* 13, 025323 (2023), 10.1063/9.0000541.
- [45] T. Moriya and A. Kawabata, Effect of Spin Fluctuations on Itinerant Electron Ferromagnetism, *J. Phys. Soc. Jpn.* 34, 639-651 (1973), 10.1143/JPSJ.34.639.
- [46] T. Moriya and A. Kawabata, Effect of Spin Fluctuations on Itinerant Electron Ferromagnetism. II, *J. Phys. Soc. Jpn.* 35, 669-676 (1973), 10.1143/JPSJ.35.669.
- [47] T. Moriya and Y. Takahashi, Spin Fluctuation Theory of Itinerant Electron Ferromagnetism –A Unified Picture, *J. Phys. Soc. Jpn.* 45, 397-408 (1978), 10.1143/JPSJ.45.397.
- [48] T. Moriya, *Spin Fluctuations in Itinerant Electron Magnetism* (Springer-Verlag, Berlin Heidelberg, Germany, 1985), Vol. 56, Springer Series in Solid-State Sciences.
- [49] Y. Takahashi, On the Origin of the Curie-Weiss Law of the Magnetic Susceptibility in Itinerant Electron Ferromagnetism, *J. Phys. Soc. Jpn.* 55, 3553-3573 (1986), 10.1143/JPSJ.55.3553.
- [50] Y. Takahashi, *Spin Fluctuation Theory of Itinerant Electron Magnetism* (Springer-Verlag, Berlin Heidelberg, Germany, 2013), Springer Tracts in Modern Physics, 253.
- [51] E. C. Stoner, Collective electron ferromagnetism, *Proc. R. Soc. A* 165, 372-414 (1938), 10.1098/rspa.1938.0066.

- [52] T. Sakon, Y. Hayashi, A. Fukuya, D. Li, F. Honda, R. Y. Umetsu, X. Xu, G. Oomi, T. Kanomata, and T. Eto, Investigation of the Itinerant Electron Ferromagnetism of  $\text{Ni}_{2+x}\text{MnGa}_{1-x}$  and  $\text{Co}_2\text{VGa}$  Heusler Alloys, *Materials* 12, 575 (2019), 10.3390/ma12040575.
- [53] S. M. Saunders, L. Xiang, R. Khasanov, T. Kong, Q. Lin, S. L. Bud'ko, and P. C. Canfield, Exceedingly Small Moment Itinerant Ferromagnetism of Single Crystalline  $\text{La}_5\text{Co}_2\text{Ge}_3$ , *Phys. Rev. B* 101, 214405 (2020), 10.1103/PhysRevB.101.214405.
- [54] P. Rhodes and E. P. Wohlfarth, The Effective Curie-Weiss Constant of Ferromagnetic Metals and Alloys, *Proc. R. Soc. A* 273, 247-258 (1963), 10.1098/rspa.1963.0086.